THE UNIVERSITY *of* EDINBURGH

Edinburgh Research Explorer

Multiple Coulomb phase in the fluoride pyrochlore CsNiCrF6

OPEN ACCESS

Multiple Coulomb phase in the fluoride pyrochlore $CsNiCrF_6$

T. Fennell[1*], M. J. Harris[2], S. Calder[3], M. Ruminy[1], M. Boehm[4], P. Steffens[4], M.-H. Lemée-Cailleau[4], O. Zaharko[1], A. Cervellino[5], S. T. Bramwell[6]

[1]Laboratory for Neutron Scattering and Imaging, Paul Scherrer Institut, 5232 Villigen PSI, Switzerland

[2]School of Divinity, University of Edinburgh, New College, Mound Place, Edinburgh, EH1 2LX, UK

[3]Quantum Condensed Matter Division, Oak Ridge National Laboratory, Oak Ridge, Tennessee 37831, USA

[4]Institut Laue-Langevin, 71 avenue des Martyrs, CS 20156, 38042 Grenoble cedex 9, France

[5]Swiss Light Source, Paul Scherrer Institut, 5232 Villigen PSI, Switzerland

[6]London Centre for Nanotechnology and Department of Physics and Astronomy, University College London, 17-19 Gordon Street, London WC1H 0AH, UK

* tom.fennell@psi.ch

The Coulomb phase is an idealized state of matter, whose properties are determined by factors beyond conventional considerations of symmetry, including global topology, conservation laws and emergent order. Theoretically, Coulomb phases occur in ice-type systems like ice and spin ice; in dimer models; and certain spin liquids. However, apart from ice-type systems, more general experimental examples are very scarce. Here we study the partly-disordered material $CsNiCrF_6$ and show that this material is a multiple Coulomb phase with signature correlations in three degrees of freedom: charge configurations, atom displacements, and spin configurations. We use neutron and x-ray scattering to separate these correlations, and to determine the magnetic excitation spectrum. Our results show how the structural and magnetic properties of apparently disordered materials may inherit, and be dictated by, a hidden symmetry – the local gauge symmetry of an underlying Coulomb phase.

44   The correlations and dynamics of conventional phases of matter can be summarized in terms
45   of broken symmetries [1] and the transverse (Goldstone) and longitudinal (Higgs) fluctuations
46   of their associated order parameters [2]. By contrast, in a Coulomb phase [3], there is no long-
47   range order and the cooperative behavior of the local degrees of freedom is best described by
48   a field, whose emergent symmetry is that of the electromagnetic field. Any ground state of the
49   local degrees of freedom can be represented by a non-divergent field (i.e. div$\mathbf{B}$=0, see Fig. 1A),
50   which means that although the Coulomb phase has no broken global symmetry, it has local
51   gauge symmetry and the closed loop topology of the associated field lines [3,4,5]. Dynamics
52   involve coherent fluctuations of the field, or topological defects in the field, which can
53   respectively be identified as generalized photons and charges of the relevant field theories
54   [6,7,8].
55
56   Although the charge ice [9,10] (Fig. 1B) and the pyrochlore Heisenberg antiferromagnet [11]
57   (Fig. 1C) are two of the best-known predicted Coulomb phases, neither has a good
58   experimental model system. Theoretical investigations of the pyrochlore Heisenberg
59   antiferromagnet highlight the generalities of Coulomb phases [11,12,13,14,15]. The spin
60   correlation function has the power-law behavior generic to all Coulomb phases, implying that
61   there should be `pinch-points' in the static structure factor [3,12,16,17]. Creation of
62   topological defects in the flux fields (monopoles, though in this case not discretized as they are
63   in spin ice [18,19,20]) modifies the magnetic charge density locally, and relaxation of this
64   disturbance leads to a monopole current. The associated spin relaxation rate depends only on
65   temperature (i.e. it exhibits E/T scaling) and occurs at many wave vectors, including the pinch
66   points, as shown by the theoretical spin relaxation function $S(\mathbf{Q},t)/S(\mathbf{Q},0)$ [14,15] illustrated in
67   Fig. 2A. On nodal lines connecting the pinch points, different behaviors are found. In a cut
68   through the simulated $S(\mathbf{Q},\omega)$ along a nodal line, as shown in Fig. 2B [15], the relaxational
69   response at the zone centre gives way to spin diffusion at small wave vectors where fluctuations
70   conserve the local magnetization; fast, quasi-dispersive dynamics due to remnant spin waves
71   appear further along the nodal lines. It was recently suggested that the lattice dynamics of
72   solids with correlated disorder (including charge ices) may be of interest for functional
73   properties such as thermoelectricity [21], but the vibrational analogs of general Coulomb phase
74   dynamics have not been investigated. Moreover, in dense spin systems with mixed cations
75   such as Y_2CrSbO_7 or $YbMgGaO_4$, site and bond disorder clearly have important consequences
76   for the magnetic properties [22,23,24]. These materials are suggested to have random disorder,
77   but although correlated disorder may be difficult to detect, it is highly probable because the
78   long-range nature of the Coulomb interaction makes it divergent in the presence of random
79   disorder. Further investigations of such materials may well emphasize the importance of
80   understanding spin systems that live on structures with correlated disorder.
81
82   In this work, we use x-ray and neutron scattering to investigate correlations and dynamics in
83     $CsNiCrF_6$, in which Ni^{2+} and Cr^{3+} jointly occupy a pyrochlore lattice. $CsNiCrF_6$ was suggested
84   to be a pyrochlore Heisenberg antiferromagnet [25,26] before the concept of a Coulomb phase
85   emerged. However, even in the simplest description [27], Ni-Ni, Ni-Cr and Cr-Cr
86   superexchange constants form a set of different values, breaking the local degeneracy of the
87   true pyrochlore Heisenberg antiferromagnet that is crucial to the formation of a Coulomb
88   phase. However, with two ions of different charge on the pyrochlore lattice, $CsNiCrF_6$ is a
89   candidate charge ice and later we show how a magnetic Coulomb phase is inherited from the
90   charge ice structural correlations.
91
92   The charge ice structure can be addressed in two ways: the average crystal structure can be
93   studied by conventional diffraction experiments, and departures from the average due to

94   (correlated) disorder can be investigated by measuring structural diffuse scattering [28]. To
95   investigate the average structure, we performed single crystal neutron diffraction and
96   synchrotron powder x-ray diffraction experiments. Refinement of crystallographic models
97   against these data indicate three features: firstly, the average structure is well described by that
98   of the mixed metal fluoride pyrochlores (see Fig. 1D,E), with isotropic displacement
99   parameters [29]; secondly, the thermal displacement factor of the Cs^+ ion is by far the largest
100   of all the atoms, and is strongly thermally activated; lastly, split site models in which ions
101   partially occupy a lower symmetry site around the expected position, as in other pyrochlore
102   materials with structural disorder [30] are not stable or do not improve the refinement. Further
103   details of the refinements are given in the supplementary information [31].

105   If there is sufficient contrast in neutron scattering length between the two cations, as is the case
106   for Ni (b_c=10.3 barn) and Cr (b_c=3.6 barn), there should be a direct signature of charge ice
107   correlations in the structural (i.e. nuclear) diffuse neutron scattering. We used polarized
108   neutron scattering to separate structural and magnetic scattering. The structural diffuse
109   scattering is shown in Fig. 3A, and its form indicates that non-trivial structural correlations are
110   present. In the experimental data the intensity of the diffuse features generally increases with
111   the magnitude of the wavevector, while a model calculation of a charge ice with only
112   substitutional correlations (Fig. 3B) has diffuse features with similar weight across the whole
113   pattern. The calculation has pinch points at (-2,-2,0) and (0,0,2), whose existence and position
114   are the defining features of a structural Coulomb phase on the pyrochlore lattice [3]. We can
115   identify one of these pinch points in the experimental data. In Fig. 3A, a triangular region of
116   intensity around (h,h,0) sharpens inward, towards (2,2,0). Cuts through the experimental data
117   (Fig. 3D) confirm that the scattering sharpens toward the (2,2,0) Bragg point, and that this
118   feature is therefore a type of pinch point. The very weak intensity of the inner part of the
119   pattern prevents us from concluding on the exact nature of the features around (0,0,2), but the
120   intense diffuse scattering pinching in toward (0,0,6) at the limit of our wave vector coverage
121   suggests another pinch point, as expected from the calculation. The pinch points are the
122   essential characteristic of the Coulomb phase, indicating the long-range coherence of the ice
123   rules, their presence in the experimental data shows unambiguously that a structural Coulomb
124   phase is present.

126   The other, more diffuse, features characterize short-wavelength correlations or local structures
127   that exist within the Coulomb phase, and the distribution of intensity in the experimental
128   pattern compared to the calculation shows that the structure contains contributions beyond
129   purely ice-rule obeying cation configurations. When working with single crystal diffuse
130   scattering data with relatively limited wave vector access, numerical modelling in direct space
131   is most convenient [32, 33, 34, 35], and we propose a simple model that explains our structural
132   observations reasonably well. From the point of view of the bond valence sum [36], the
133   average structure is an efficient compromise: no cation has a fully favorable bond valence sum,
134   but all are close to their optimal values. If ice rule cation correlations exist amongst Ni^{2+} and
135   Cr^{3+}, we can make a local distortion throughout the structure (Fig. 1D) that brings the bond
136   valence sum of both cations to their optimal values. The Ni/Cr cations have octahedral
137   coordination, sharing four F^- with cations of the other type and two with cations of the same
138   type. We assume only that any F^- shared between a Ni^{2+}-Cr^{3+} pair is displaced (always by the
139   same amount) toward the Cr^{3+}, sufficient to simultaneously optimize the bond valence sum of
140   all Ni^{2+} and Cr^{3+} ions. The displacement is small enough to lie within the radius of the isotropic
141   displacement parameter, consistent with the absence of a split site in structural refinements or
142   Fourier difference maps. Then, if we search for the locus of sites optimizing the bond valence
143   sum for each Cs^+, we find it takes the form of one or more connected loops on the surface of a

144 sphere, with the average over all Cs^+ sites making a hollow spherical shell. As in other such
145 cases, the radius of the shell is larger than the displacement parameter of the atom in the average
146 structure [37].

148 The introduction of the cation correlations and local distortion of the octahedra has a strong
149 effect on the calculated structural diffuse scattering - the local distortions redistribute the
150 weight of the pure configurational disorder pattern towards larger wave vector, suppressing the
151 part in the center of the pattern (Fig. 3C) but leaving the pinch point at (2,2,0) described above.
152 Furthermore, the combination of cation correlations and local anion displacements modifies
153 the topology of the available Cs^+ positions from discrete pockets in the average structure (i.e.
154 a split site), to continuous displacements on the surface of a sphere, which on average resembles
155 a large, isotropic displacement parameter as observed. If the framework cations are random,
156 the local distortions still improve the bond valence sums, and still have the same effect on the
157 Cs^+ displacement topology, but the diffuse scattering is a featureless response from the random
158 cations convoluted with weighting to larger wave vector due to the displacements.

160 Every tetrahedron has four edges with a displacement and two without, a condition that can
161 readily be represented by an ice rule on a single tetrahedron, but the relationship between ice
162 rule and fluxes requires a sign change in `up' and `down' tetrahedra, since anions are displaced
163 toward a cation in both of the tetrahedra of which the cation is a member. An alternative
164 identification of the Coulomb phase in the displacements can be made: the edges of the
165 tetrahedra with a non-displaced F^- anion (or matching cations at each end) select two of the
166 links of the diamond lattice that terminate at the diamond lattice point at the center of the
167 tetrahedron (Fig. 1D); each cation is a member of another such pair on adjacent tetrahedra,
168 similarly selecting two diamond lattice links on these tetrahedra (Fig. 1D, E); tracing the
169 network of diamond lattice links selected in this way reveals a fully packed loop model. Every
170 link of the diamond lattice is a member of a loop and each diamond lattice point is visited by
171 precisely two loops; a given loop is populated only by one type of cation. The same fully
172 packed loop model is obtained by coloring, in two colors, the links of the diamond lattice that
173 host in or out spins in a spin ice [38]. Fully packed loop models represent an intriguing type
174 of correlated disorder, which has so far found experimental relevance only in two dimensions
175 [39,40]. In $CsNiCrF_6$, this displacement ice must play an important role in the exchange
176 interactions and their disorder. The ideal pyrochlore Heisenberg antiferromagnet has a single
177 exchange parameter, but here we can expect three, one each for Ni-Ni, Ni-Cr and Cr-Cr bonds.
178 The required theory will not be one of random disorder of exchange strengths, but of a strongly
179 correlated spatial distribution of exchanges, whose structure is encoded by the fully packed
180 loop model [27].

182 Our model does not reproduce every aspect of the structural diffuse scattering pattern, but the
183 form of the experimental data and improvements made over the simple charge ice calculation
184 suggest the basic ingredients – a charge ice of Ni^{2+} and Cr^{3+}, displacements of the F^- anions that
185 inherit Coulomb phase correlations from the underlying charge ice, and Cs^+ ions disordered
186 over the surface of a spherical shell around the cage centers – are correct. However, the model
187 is very simple: the ice rules are assumed to operate perfectly (some additional consideration of
188 this point can be found in the supplementary information [31]), with complete degeneracy
189 amongst all microstates (which is known not to be the case in spin ice); the same F^-
190 displacement is made throughout the structure, irrespective of the symmetry of the local
191 distortion - $O_h \rightarrow D_{4h}$ and $O_h \rightarrow C_{2v}$ may both occur depending on the configuration of
192 displaceable F^- ions around each Cr^{3+} and may in reality be differently favorable; and the Cs^+
193 ions are completely decoupled from the framework.

194

195 From the point of view of magnetism, the Curie-Weiss temperature (-70 K) suggests that in
196 CsNiCrF$_6$, the magnetic moments of two sizes (Ni^{2+} has S=1, Cr^{3+} has S=3/2) distributed
197 according to the ice rules, interact antiferromagnetically on average. Separation of the
198 magnetic diffuse scattering by polarized neutron scattering shows that the spins also form a
199 Coulomb phase. The static magnetic correlations exposed in a measurement of $S(\mathbf{Q})$ contain
200 pinch points, and a distribution of intensity similar to the pyrochlore Heisenberg
201 antiferromagnet, as shown in Fig. 4A and B. The existence of pyrochlore Heisenberg
202 antiferromagnet-like correlations in a system with two different interacting ions (distributed
203 according to the ice rules/fully packed loop model) has been justified by numerical simulations
204 for an extensive range of interaction parameters (see regime IV in Ref. [27]). It is clear from
205 our results that CsNiCrF$_6$ falls within this range. As discussed in Ref. [27], the Coulomb phase
206 correlations of the spin system are here inherited from the underlying structural Coulomb phase
207 and do not reflect the degeneracy of the Heisenberg manifold.

208

209 This conclusion is supported by a study of the magnetic dynamics using inelastic neutron
210 scattering. Previous studies have shown that there is considerable spectral weight at an energy
211 transfer of ~0.5 meV [26], and in Fig. 5A we show a map of the intensity at constant energy
212 transfer of 0.5 meV. This measurement shows that the spin fluctuations have a structure factor
213 very similar to the static correlations of the Coulomb phase, implying degenerate fluctuations
214 of both long and short wavelength. Constant wave vector scans were used to further investigate
215 the form of $S(\mathbf{Q},\omega)$. The locations of these scans are summarized in Fig. 2A, they probe the
216 nodal lines ($h,h,-h$) and ($0,0,l$), including pinch points at ($1,1,-1$) and ($0,0,-2$), and generic points
217 on the intense structure factor of Fig. 5A. In Fig. 5B, we show scans measured at the pinch
218 points and generic points. We have converted $S(\mathbf{Q},\omega)$ to $\chi''(\mathbf{Q},\omega)$ in order to simplify model-
219 free interpretations. The data from all these points can be fitted by gapless quasi-elastic
220 Lorentzians with the same width, indicating that the relaxation rate is independent of wave
221 vector (but the intensity varies with position, as expected from Fig. 5A). In Fig. 5C we show
222 a series of scans along a nodal line from a pinch point at ($1,1,-1$) toward the adjoining regions
223 with no scattering in Fig. 5A (i.e. ($0,0,0$) or ($2,2,-2$)). Here we see that the gapless behavior at
224 the pinch point is preserved at small wave vector relative to the pinch point (e.g. ($1.1,1.1,-1.1$),
225 but a broad peak with a distinct dispersion appears beyond this. Beyond ($1.5,1.5,-1.5$), the peak
226 becomes very weak and much broader, dispersing back downward as far as it can be followed.
227 The temperature dependence of the width of the susceptibility at two generic wavevectors is
228 linear with the temperature, as shown in Fig. 5D, with a finite response at the lowest
229 temperature. The width of the dispersive feature has essentially the same temperature
230 dependence. In Fig. 5E we summarize our data for nodal lines, showing the sinusoidal
231 dispersion of the fast dynamics.

232

233 CsNiCrF$_6$ affords the possibility of studying the dynamics of a magnetic Coulomb phase with
234 full wave vector and frequency information. Interestingly, many features of these dynamics
235 are similar to those of the classical spin liquid phase of the pyrochlore Heisenberg
236 antiferromagnet. In particular, monopole current density is signified by the wave vector-
237 independent relaxation rate with linear temperature at generic wave vectors [14]. Along the
238 nodal lines, the response at and close to the pinch point is gapless. This is consistent with the
239 presence of relaxational dynamics at the pinch point and diffusional dynamics at small wave
240 vector but more extensive measurements would be required to confirm the expected data
241 collapse for spin diffusion. We clearly see a feature that disperses up from the pinch point.
242 The dispersion on the nodal lines is periodic with respect to the pinch points (and identical for
243 the two nodal lines). When compared qualitatively with the prediction of Fig. 2B [14, 15], the

observation of a quasi-linear or sinusoidal dispersion up to the maximum, followed by a collapse into a very broad, weak and downward dispersing intensity is as expected. This dispersive feature represents a fast contribution to the dynamics that can be thought of as a spin wave fluctuation about the local ground state. It is broad in both wave vector and energy since the ground state is not ordered [14].

It may seem remarkable that the delicate-sounding predictions of the pyrochlore Heisenberg antiferromagnet are robust to the strongly correlated structural disorder that we have also described. However, the fully packed ion loops of a charge ice still give rise to a magnetic Coulomb phase of antiferromagnetic character [27], and conserved or topological quantities are closely related to those of the Heisenberg model, leading to similar emergent physics. The expected clear departure from the classical pyrochlore Heisenberg antiferromagnet behavior is, however, manifest in the temperature dependence of the relaxation rate at the generic wavevectors. This quantity is predicted to be simply proportional to the temperature and vanish as $T \rightarrow 0$ [14,15], but we find a weaker temperature dependence and residual response at the lowest temperature.

Below $T=2.3$ K magnetization measurements on $CsNiCrF_6$ exhibit a history dependence that is reminiscent of canonical spin glasses [25]. A slowing component of dynamics that coexists with the processes we measure here, and which falls into the time window of a magnetization experiment at this temperature seems by no means inconsistent with Ref. [25], but the significant inelastic spectral weight that we observe both above and far below this temperature precludes that $CsNiCrF_6$ is a canonical spin glass [25,26]. Given the relatively small spin sizes, the lowest temperature response may indicate that a quantum spin liquid [41] replaces the classical one.

We have shown that $CsNiCrF_6$ supports multiple Coulomb phases – a charge ice and associated displacement ice, and a magnetic Coulomb phase with antiferromagnetic character. Despite being composed of fully-packed loops of distinct spins, the magnetic Coulomb phase shows dynamical signatures of the pyrochlore Heisenberg antiferromagnet, a classical spin liquid of much higher local symmetry. Our results show how two systems that look completely different from a structural chemistry perspective, may nevertheless share many of the same physical properties, the key connection being the robust local gauge symmetry of the Coulomb phase and its associated conservation laws.

Predictions of wave vector-dependent dynamics of a classical antiferromagnetic Coulomb phase have not previously been examined experimentally (although we note very recent work on a possible quantum analogue, $NaCaNi_2F_7$ [42]). The consequences of ice-rules disorder in the vibrational dynamics (of the framework) have not been examined experimentally or theoretically, but the interplay of framework and caged-atom dynamics are well known to contribute to advantageous thermoelectric properties in skutterudite and clathrate compounds such as $CeFe_4Sb_{12}$ [43], and superconductivity in the analogously structured osmate pyrochlores such as KOs_2O_6 [44]. The chemical flexibility of the fluoride pyrochlore crystal structure (which includes the possibilities of significantly varying the magnetic properties with numerous combinations of transition metal cations, replacing the alkali metal cation with a guest of quite different character such as NH_4^+, or extracting it, as in FeF_3, and of exploring charge ordered versions using compositions such as AFe_2F_6 [45,46], perhaps with a view to metallization) suggests that these compounds are of considerable interest for exploration of both unconventional spin dynamics, and new functionalities based on correlated disorder.

293
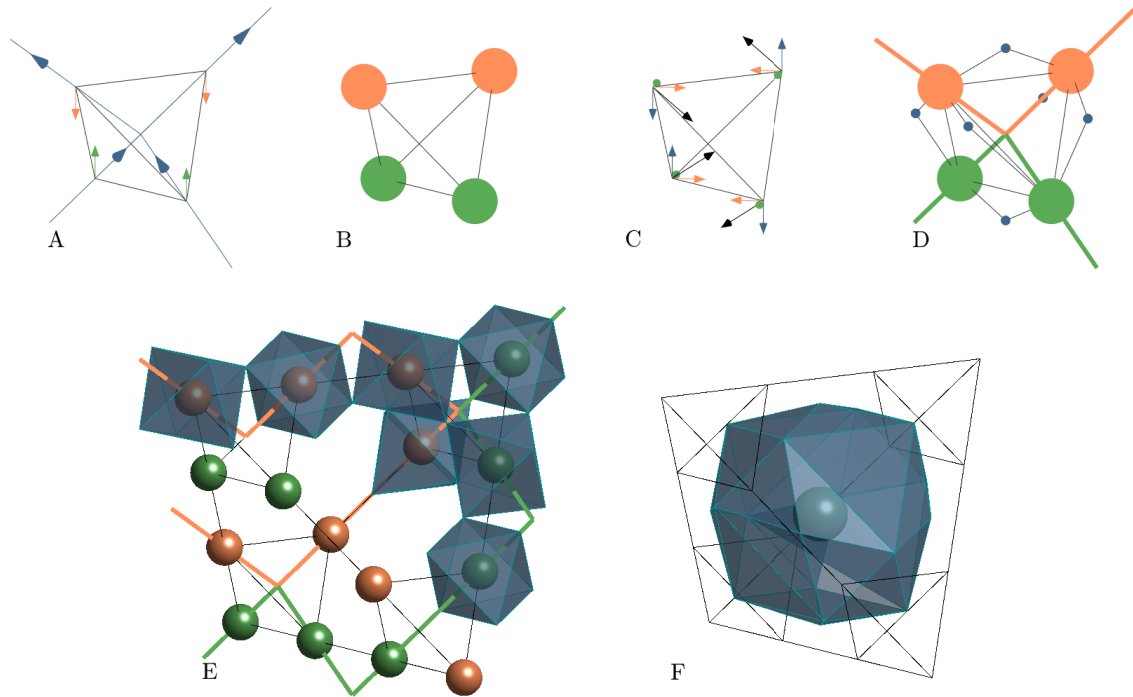
Fig. 1. Illustration of Coulomb phase construction/mappings and structural features of CsNiCrF$_6$. A: The pyrochlore lattice (medial) consists of corner-sharing tetrahedra, on which a Coulomb phase is established when the local degrees of freedom can be represented by a non-divergent field derived from lattice fluxes on the diamond lattice (parent) [3]. A non-divergent configuration of flux variables (blue arrows) around a diamond lattice point is equivalent to the ice rule for spins in a spin ice (two-in-two-out). Antiferromagnetic pseudo-spins are related to the flux variables and configured two-up-two-down in a Coulomb phase ground state (green and orange arrows). B: Two cations occupying the pyrochlore lattice form a charge ice, with cation configurations directly related to the pseudo-spins (green and orange spheres). C: Vector spins coupled antiferromagnetically on the pyrochlore lattice (i.e. a pyrochlore Heisenberg antiferromagnet) must satisfy the condition that the total magnetization of every tetrahedron is zero (black arrows), which can be ensured if the $S_{x,y,z}$ vector components are each represented by a family of pseudospins that obey the ice rule (blue, green and orange arrows). D: In the structure of CsNiCrF$_6$, F$^-$ anions (small blue spheres) are coordinated to two cations (orange spheres are Cr^{3+}, green spheres are Ni^{2+}). The bond valence sum requirements of the cations can be satisfied by displacing anions shared by a pair of unlike cations towards the cation with larger charge (Cr^{3+}). Anions shared between a pair of like cations are not displaced. The edges with non-displaced anions form a fully packed loop model (described in text) on the diamond lattice (green and orange lines). E: The structure of CsNiCrF$_6$ is composed of the pyrochlore lattice of cations, coordinated by octahedra of F$^-$ ions. The octahedra share each of their vertices with another octahedron, forming tetrahedra of tilted octahedra. (Extended sections of the fully packed loop model are shown and the octahedra are drawn undistorted.) F: The structure contains large cages in which the Cs$^+$ ions reside. The cage coordination is by 18 F$^-$ ions, forming an octahedron that is truncated and capped with rectangular pyramids.

319

320

321
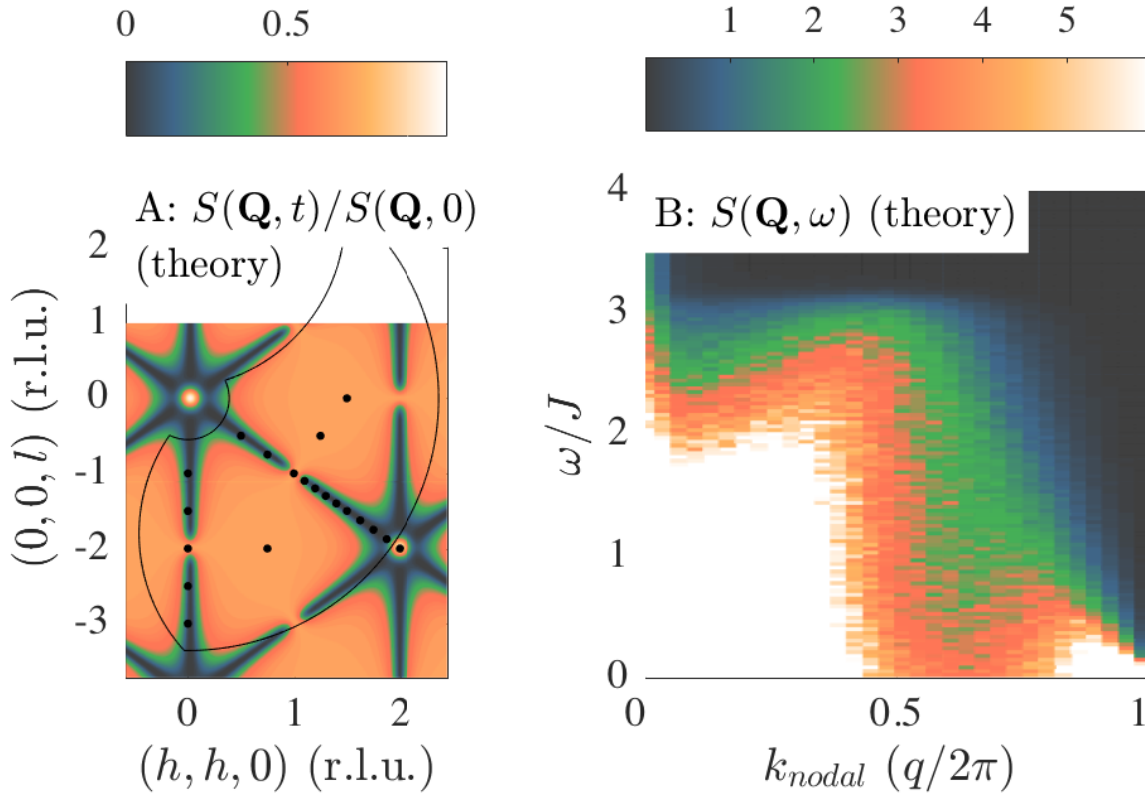
Fig. 2. Illustration of theoretical predictions of the dynamical response of the pyrochlore Heisenberg antiferromagnet. The relaxation function $S(\mathbf{Q},t)/S(\mathbf{Q},0)$ (from [15]) has large regions of reciprocal space where identical relaxation times are expected. The normalization highlights that the scattering function at these wavevectors will have the same width, even if their structure factor is different. The nodal lines, where different dynamical regimes are found, can be clearly seen. The extent (curved lines) and positions (dots) of our mapping and scanning measurements are also shown. B: A sketch of the spectrum along a nodal line (i.e. $(h,h,-h)$) (from [15]) shows the crossovers from gapless relaxational dynamics at the pinch point ($\mathbf{k}_{nodal}$=0), to gapless diffusional dynamics at small $|\mathbf{k}|$, to quasi-dispersive fast dynamics toward $|\mathbf{k}|$=0.5, with broad and weak signal for $|\mathbf{k}|$>0.5.

342

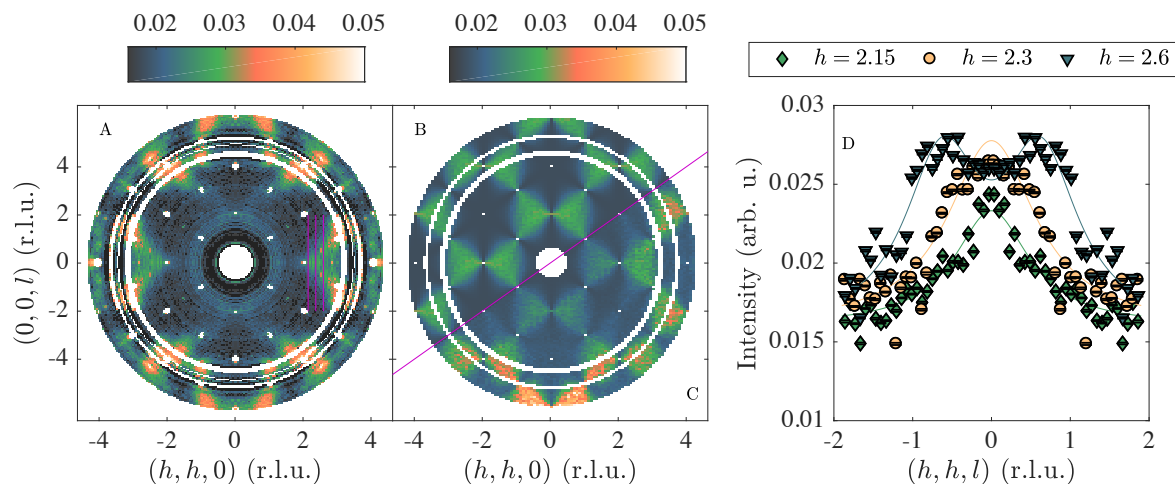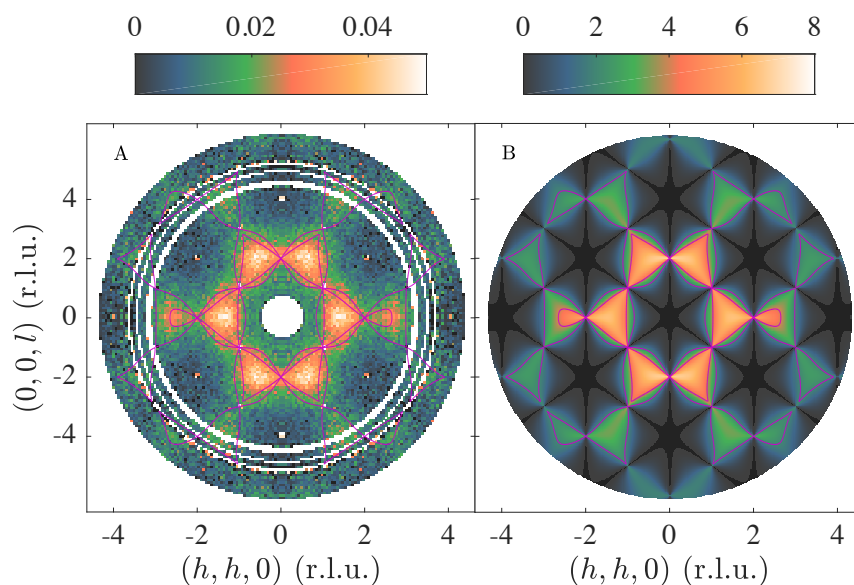**Fig. 3**. Structural diffuse scattering in CsNiCrF$_6$. A: The structural diffuse neutron scattering measured at 1.5 K (note that the colour scale starts at 0.01 (arbitrary units) to highlight the weak diffuse scattering around (1,1,1) and (0,0,2), there is a significant wavevector independent diffuse contribution which may arise from isotope incoherent scattering, uncorrelated Cs$^+$ ions, and/or ice rule defects). B: Predicted diffuse scattering of a charge ice with substitutional correlations only. C: Diffuse scattering calculated for a model with charge ice cation correlations and associated bond valence sum-restoring F$^-$ and Cs$^+$ displacements. In B and C the calculated intensity is multiplied by a scale factor and a wavevector independent contribution added. D: Cuts through the experimental data (positions indicated by lines on A) show that the feature around (h,h,0) sharpens inward toward the (2,2,0) position, and is, therefore, the pinch point visible at that position in B and C. Error bars in D are obtained by standard propagation of the Poisson counting statistics of all the measurements (sample, background, calibrants) required to extract the structural scattering cross section.

356

Fig. 4. Magnetic diffuse scattering in CsNiCrF$_6$. A: The experimental magnetic diffuse neutron scattering measured at 1.5 K. B: Model calculation of the structure factor of the pyrochlore Heisenberg antiferromagnet (including the average magnetic form factor for Ni^{2+} and Cr^{3+}) [16]. The calculation is for T=0 and incorporates no structural disorder or modulation of the magnetic moment size by site, so its pinch points are extremely sharp and better defined than

those in the experimental data. Isointensity contours from the calculation are superimposed on
the experimental data as guides to the eye.
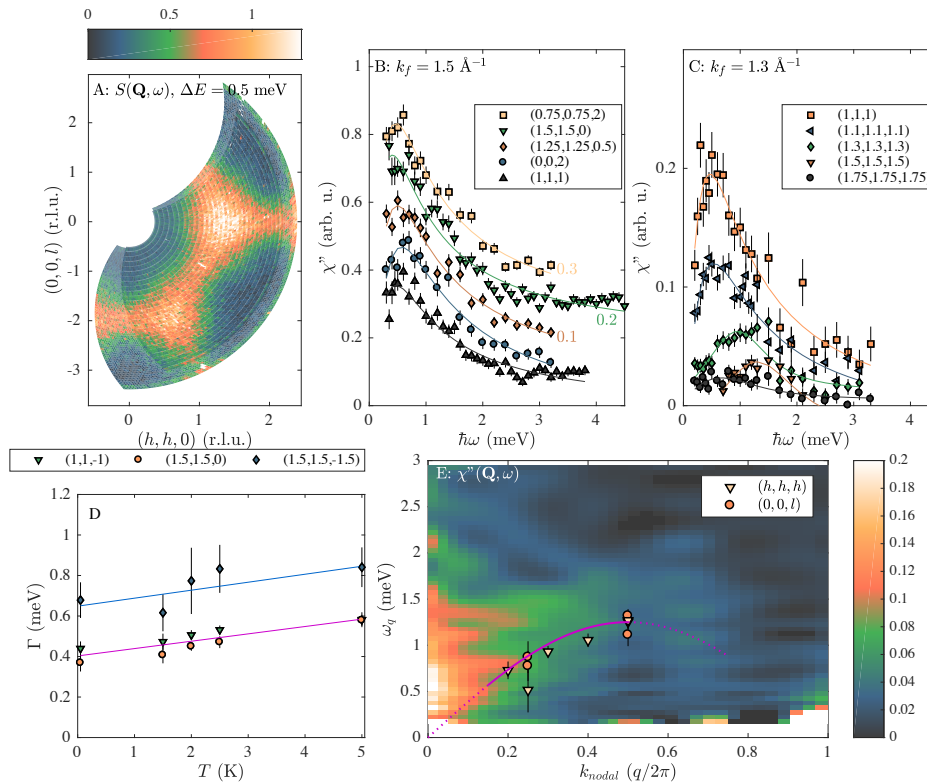
Fig. 5. Wave vector and temperature dependence of magnetic dynamics in CsNiCrF$_6$. A: A map of $S(\mathbf{Q},\omega)$ at a constant energy transfer of 0.5 meV shows a structure factor very similar to the static correlations shown in Fig. 4, but with broadened pinch points. B: Constant wave vector scans at pinch points and points on the structure factor of panel A where relaxational dynamics are expected (see Fig. 2) all have the same width (small numbers adjacent to a data series indicate an arbitrary offset that has been applied to help distinguish them, the real intensity of these series is essentially identical, lines are fits to a gapless quasielastic Lorentizan line shape). C: Constant wave vector scans along the nodal line ($h,h,-h$) show a gapless spectrum at small |kl|, followed by an upward dispersive peak for $0.2<|kl|<0.5$, followed by broad, weak signals of decreasing intensity (lines are fits to a damped harmonic oscillator line shape with pole at finite energy). D: The width of the relaxational dynamics signal is linear in T, with a significant intercept at low temperature. The width of the dispersive peak at (1.5,1.5,-1.5) has an essentially identical temperature dependence. E: Summary of the nodal line dynamics, showing gapless behavior close to the pinch point, replaced by dispersive fast dynamics and weak broad scattering. The points and line indicate the dispersion of the susceptibility peak along both nodal lines and in both directions from the pinch point, folded into reduced units. The color map is an interpolation of the susceptibility measured in the constant wave vector scans (along ($h,h,-h$)). Error bars in B and C are derived from Poisson counting statistics of the measurement with scaling from $S(\mathbf{Q},\omega)$ to $\chi''(\mathbf{Q},\omega)$. Error bars in D and E are the uncertainties of the least squares fitted parameters.

Materials and Methods [References 47-56]**:**

Our main sample is a single crystal of $CsNiCrF_6$, used and described in [25,26]. It is roughly cuboidal, with dimensions $\approx$6x8x12 mm. It was aligned by neutron Laue diffraction using Orient Express at the Institut Laue Langevin (ILL) (Grenoble, France) and mounted according to the intended experiment: glued to an aluminum finger with Quikfill (epoxy) for inelastic neutron scattering experiments at T>1.5 K; glued to a copper finger with Stycast (epoxy) for inelastic neutron scattering experiments at T< 1 K; wrapped in aluminum foil that was clamped to an aluminum finger for polarized diffuse neutron scattering experiments. Small pieces of dimension $\approx$0.5x1x2 mm that broke off the surface of the sample during ungluing were preserved and used for single crystal neutron diffraction experiments (glued to aluminum pins using Quikfill or GE varnish) or crushed for powder x-ray diffraction. We have a second crystal that has a well-developed octahedral form with edge dimension $\approx$5 mm. A small piece cut from this was also examined by x-ray powder diffraction.

For our synchrotron x-ray powder diffraction experiments, a piece of either crystal was mixed with silicon powder and ground together in an agate pestle and mortar. These mixtures were loaded into 0.3 mm glass capillaries. The silicon serves primarily to disperse small sample volume in the beam, and also provides a convenient calibrant for wavelength and lattice parameters (a_{Si}=5.431194 Å at 22.5°C, NIST powder diffraction standard 640c). We used the high-resolution powder diffractometer of the Materials Science Beamline [47] at the Swiss Light Source (SLS) (Paul Scherrer Institut, Villigen, Switzerland) to measure the diffraction pattern of the mixture. The diffractometer was operated in Debye-Scherrer geometry with Mythen microstrip detector and capillary spinner, the wavelength was 0.4959 Å (25 keV). The 2θ range extended from 7° to 120° without cryostat, or 7° to 80° with helium flow cryostat installed. We collected diffraction patterns at room temperature (24°C at the SLS) without the cryostat for the main sample, and between 5 K and 300 K with the cryostat for both. The powder diffraction data were normalized and reduced by standard routines, then modeled and fitted using the Rietveld method, as implemented in the package FullProf [47].

We carried out a single crystal neutron diffraction experiment using the quasi-Laue diffractometer VIVALDI [49] at the ILL. The sample was mounted in an `Orange' helium cryostat and cooled to $T\approx$2.5 K. To ensure a full coverage of reciprocal space, the sample was rotated through 180° about the vertical axis, with 1-hour duration exposures recorded every 10°. The data were indexed and integrated using the program LAUEGEN [50], and wavelength normalized using LAUENORM [51]. The resulting integrated intensities were used for least squares refinement of crystallographic models using the package ShelXL [52]. A second single crystal neutron diffraction experiment was carried out using the monochromatic diffractometer TRiCS [53] at the Swiss Spallation Neutron Source (SINQ) (Paul Scherrer Institut, Villigen, Switzerland) in 4-circle mode. The sample was attached to the cold finger of a closed cycle cooling machine that was mounted on the Euler cradle. Using the germanium (Ge311) monochromator to provide neutrons of wavelength of 1.172 Å and a single ^{3}He tube detector, we measured 2550 reflections, with the temperature T=5 K throughout. Integrated intensities were combined and used for least squares refinement of crystallographic models using the packages Jana2000 and FullProf [54,47].

We measured and separated the magnetic and structural diffuse neutron scattering using the polarized neutron diffuse scattering spectrometer D7 [55] at the ILL. D7 was configured with wavelength λ=3.1 Å and Orange cryostat. The sample was mounted using aluminum foil to minimize incoherent scattering from glue, two strong Bragg peaks from the tails of the cryostat

436 contaminate the data and these areas are masked in the data analysis. We used the XYZ
437 technique, which requires the measurement of non-spin flip and spin flip intensities for three
438 orthogonal polarization directions, to separate the structural, spin incoherent, and magnetic
439 cross sections. We rotated the crystal about the vertical axis in 0.5° steps, recording three
440 complete rotations with the analyzer/detector banks offset in three non-overlapping positions
441 and 17-18 s count time per channel, plus a further 270° rotation in one of the detector positions
442 with 20 s count time. The sample was maintained at $T{\approx}1.8$ K throughout. We measured the
443 background of the empty sample holder for each of the three detector positions with coarse
444 rotation steps (18° or 30°) and 60 s counting times. The background was essentially angle
445 independent so measurements at different rotation angles were combined and duplicated for
446 subtraction from the sample data. Standard vanadium and quartz (silica glass) samples were
447 used for normalization of detector and polarization analyzer efficiencies respectively. The
448 nuclear, magnetic and spin incoherent cross sections were separated [55] and symmetrized by
449 folding into a single quadrant of the scattering plane and then unfolding.

451 We report data from three inelastic neutron scattering experiments performed using the cold
452 neutron triple axis spectrometer IN14 at the ILL. In the first, the sample was mounted in an
453 Orange cryostat and cooled to $T{\approx}1.8$ K. The instrument was configured with PG002
454 monochromator and FlatCone analyzer. The FlatCone analyzer has 31 silicon (1,1,1) analyzer
455 crystals, allowing to map the excitation spectrum at a single energy transfer. We recorded a
456 145° rotation of the sample (in 1° steps) with the analyzer bank offset at two positions. A
457 measurement of the incoherent scattering from a vanadium sample was used to normalize the
458 efficiency of the analyzer-detector channels. We performed two experiments in the
459 conventional triple axis configuration with PG002 monochromator and analyzer. In one, the
460 sample was cooled using the Orange cryostat, and our main collection of constant-wave vector
461 scans at various reciprocal lattice positions and temperatures was made. In the other, the sample
462 was cooled using a dilution refrigerator insert in the Orange cryostat to reach $T{\approx}0.07$ K, and a
463 limited collection of scans was made. We estimate the energy resolution at the elastic line to
464 be $\Delta E{\approx}0.1$ meV when $k_f{=}1.5$ Å^{-1} and $\Delta E{\approx}0.06$ meV when $k_f{=}1.3$ Å^{-1}.

466 Our numerical model of the structural diffuse scattering was encoded specifically by ourselves.
467 The average crystal structure is built in a cubic supercell of the pyrochlore unit cell of size
468 $L{=}6,12$. We establish an ice rule configuration of cations on the pyrochlore lattice by first
469 tiling it with hexagonal loops (supercell sizes of $L{=}6,12$ are required to ensure complete
470 coverage, such a tiling is illustrated in Ref. [56]). Starting in the lowest layer of the lattice, a
471 hexagon-loop covering is constructed with probabilistic choice between two possible origins.
472 On moving up to the next layer where sites are not covered by hexagons, the layer configuration
473 is again chosen probabilistically. Once every site of the whole lattice is assigned to a hexagon,
474 the covering can be permuted, again probabilistically, so that each possible growth direction of
475 the hexagon coverage is equally represented. Within individual hexagons sites are assigned
476 alternating up/down pseudo-spins, again choosing probabilistically between the two possible
477 configurations. At this point, a specific ice-rule obeying pseudo-spin configuration has been
478 generated, but one which does not have power-law correlations. The full power-law correlation
479 function is obtained by propagating a large number of loop moves, allowing loops of any length
480 and winding loops. Simulation of the magnetic neutron scattering pattern using spin
481 configurations generated in this way will result in the $T{=}0$ scattering pattern of the pyrochlore
482 Heisenberg antiferromagnet or spin ice, depending which type of spin is associated with the
483 pseudo-spin configuration. For the structural simulation, pseudospin orientation is converted
484 into cation identity, and we identify those tetrahedron edges with mixed cation pairs and shift

the relevant F^- anion towards its neighboring Cr^{3+} cation. Calculation of the bond valence sums at this point reveals universal satisfaction of the requirements of Ni^{2+} and Cr^{3+}, but Cs^+ remains unsatisfied. We search systematically around every cage center for positions that satisfy the Cs^+ bond valence sum, within a certain tolerance, and with a certain resolution in spherical polar coordinates, and tabulate all these positions. Then we choose positions for each Cs^+ randomly from its list and calculate the scattering pattern. The calculated data shown in Fig. 2B were obtained by repeating this procedure 200 times with $L=12$. The model intensities are scaled and a constant background added to compare with the experimental data.

Author notes: TF, MJH, SC, MB, PS, and STB carried our inelastic neutron scattering experiments; TF, M.-HL-C, and OZ carried out neutron diffraction experiments; MR and AC carried out x-ray diffraction experiments; TF analyzed all data and made calculations; TF, MJH, and STB wrote paper in collaboration with all other authors.

References and Notes:

1. L. D. Landau, E. M. Lifshitz, Statistical Physics (Pergamon, New York, 1980).

2. D. Pekker, C. M. Varma, Amplitude/Higgs Modes in Condensed Matter Physics. Annual Review of Condensed Matter Physics, **6**, 269–297 (2015).

3. C. L. Henley, The "Coulomb phase" in frustrated systems. Annual Review of Condensed Matter Physics **1**, 179–210 (2010).

4. L. D. C. Jaubert, M. J. Harris, T. Fennell, R. G. Melko, S. T. Bramwell, P. C. W. Holdsworth, Topological-Sector Fluctuations and Curie-Law Crossover in Spin Ice. Physical Review X **3**, 011014 (2013).

5. D. Huse, W. Krauth, R. Moessner, S. L. Sondhi, Coulomb and liquid dimer models in three dimensions. Physical Review Letters **91**, 167004 (2003).

6. M. Hermele, M. P. A. Fisher, L. Balents, Pyrochlore photons: The U(1) spin liquid in a $S=1/2$ three-dimensional frustrated magnet, Physical Review B **69**, 064404 (2004).

7. O. Benton, O. Sikora, N. Shannon, Seeing the light: Experimental signatures of emergent electromagnetism in a quantum spin ice. Physical Review B **86**, 075154 (2012).

8. M. J. P. Gingras, P. A. McClarty, Quantum spin ice: a search for gapless quantum spin liquids in pyrochlore magnets. Reports on Progress in Physics **77**, 056501 (2014).

9. P. W. Anderson, Ordering and antiferromagnetism in ferrites. Physical Review **102**, 1008–1013 (1956).

529 10. P. A. McClarty, A. O'Brien, F. Pollmann, Coulombic charge ice. Physical Review B
530 **89**, 195123 (2014).

531 11. R. Moessner, J. T. Chalker, Properties of a classical spin liquid: The Heisenberg
532 pyrochlore antiferromagnet, Physical Review Letters **80**, 2929–2932 (1998).

533 12. S. V. Isakov, K. Gregor, R. Moessner, S. L. Sondhi, Dipolar spin correlations in
534 classical pyrochlore magnets. Physical Review Letters **93**, 167204 (2004).

535 13. R. Moessner, J. T. Chalker, Low-temperature properties of classical geometrically
536 frustrated antiferromagnets. Physical Review B **58**, 12049–12062 (1998).

537 14. P. H. Conlon, J. T. Chalker, Spin Dynamics in Pyrochlore Heisenberg
538 Antiferromagnets. Physical Review Letters **102**, 237206 (2009).

539 15. P. H. Conlon, "Aspects of Frustrated Magnetism", thesis, Oxford University, Oxford
540 (2010).

541 16. C. L. Henley, Power-law spin correlations in pyrochlore antiferromagnets. Physical
542 Review B **71**, 014424 (2005).

543 17. T. Fennell, P. P. Deen, A. R. Wildes, K. Schmalzl, D. Prabhakaran, A. T. Boothroyd,
544 R. J. Aldus, D. F. McMorrow, S. T. Bramwell, Magnetic Coulomb Phase in the Spin Ice
545 $Ho_2Ti_2O_7$. Science **326**, 415–417 (2009).

546 18. M. J. Harris, S. T. Bramwell, D. F. McMorrow, T. Zeiske, K. W. Godfrey, Geometrical
547 Frustration in the Ferromagnetic Pyrochlore $Ho_2Ti_2O_7$. Physical Review Letters **79**, 2554–
548 2557 (1997).

549 19. C. Castelnovo, R. Moessner, S. L. Sondhi, Magnetic monopoles in spin ice. Nature
550 **451**, 42–45 (2008).

551 20. I. A. Ryzhkin, Magnetic relaxation in rare-earth oxide pyrochlores. Journal of
552 Experimental and Theoretical Physics **101**, 481–486 (2005).

553 21. A. R. Overy, A. B. Cairns, M. J. Cliffe, A. Simonov, M. G. Tucker, A. L. Goodwin,
554 Design of crystal-like aperiodic solids with selective disorder–phonon coupling. Nature
555 Communications **7**, 10445 (2016).

556 22. L. Shen, C. Greaves, R. Riyat, T. C. Hansen, and E. Blackburn, Absence of magnetic
557 long-range order in Y_2CrSbO_7: Bond-disorder-induced magnetic frustration in a
558 ferromagnetic pyrochlore, Physical Review B **96**, 094438 (2017).

559 23. Y. Li, D. Adroja, R. I. Bewley, D. Voneshen, A. A. Tsirlin, P. Gegenwart, and Q.
560 Zhang, Crystalline Electric-Field Randomness in the Triangular Lattice Spin-Liquid
561 $YbMgGaO_4$, Physical Review Letters **118**, 107202 (2017).

562 24. Z. Zhu, P. A. Maksimov, S. R. White, and A. L. Chernyshev, Disorder-Induced
563 Mimicry of a Spin Liquid in YbMgGaO4, Physical Review Letters **119**, 157201 (2017).

564 25. M. J. Harris, M. P. Zinkin, T. Zeiske, Magnetic excitations in a highly frustrated
565 pyrochlore antiferromagnet. Physical Review B **52**, R707–R710 (1995).

566 26. M. P. Zinkin, M. J. Harris, T. Zeiske, Short-range magnetic order in the frustrated
567 pyrochlore antiferromagnet $CsNiCrF_6$. Physical Review B **56**, 11786–11790 (1997).

568 27. S. T. Banks, S. T. Bramwell, Magnetic frustration in the context of pseudo-dipolar
569 ionic disorder. EPL (Europhysics Letters) **97**, 27005 (2012).

28. D. A. Keen, A. L. Goodwin, The crystallography of correlated disorder. Nature **521**, 303–309 (2015).

29. D. Babel, G. Pausewang, W. Viebahn, Die Struktur einiger Fluoride, Oxide und Oxidfluoride AMe_2X_6 der $RbNiCrF_6$-Typ. Zeitschrift fuer Naturforshung, Teil B. Anorganiche Chemie, Organishe Chemie **22**,1219-1220 (1967).

30. D. P. Shoemaker, R. Seshadri, A. L. Hector, A. Llobet, T. Proffen, C. J. Fennie, Atomic displacements in the charge ice pyrochlore $Bi_2Ti_2O_6O'$ studied by neutron total scattering. Physical Review B **81**, 144113 (2010).

31. See supplementary information.

32. T. R. Welberry, B. D. Butler, Interpretation of diffuse X-ray scattering via models of disorder. Journal of Applied Crystallography **27**, 205–231 (1994).

33. R. B. Neder, T. Proffen, "Diffuse Scattering and Defect Structure Simulations: A cook book using the program DISCUS" (Oxford University Press, Oxford, 2008).

34. J. A. M. Paddison, A. L. Goodwin, Empirical Magnetic Structure Solution of Frustrated Spin Systems. Physical Review Letters **108,** 017204 (2012).

35. S. J. L. Billinge, I. Levin, The Problem with Determining Atomic Structure at the Nanoscale. Science **316**, 561–565 (2007).

36. I. D. Brown, Recent Developments in the Methods and Applications of the Bond Valence Model. Chemical Reviews **109**, 6858-6919 (2009).

37. V. V. Chernyshev, S. G. Zhukov, A. V. Yatsenko, L. A. Aslanov, and H. Schenk, The use of Continuous Atomic Distributions in Structural Investigations. Acta Crystallographica Section A: Foundations of Crystallography **50**, 601–605 (1994).

38. L. D. C. Jaubert, M. Haque, R. Moessner, Analysis of a Fully Packed Loop Model Arising in a Magnetic Coulomb Phase, Physical Review Letters **107**, 177202 (2011).

39. M. O. Blunt, and J. C. Russell, M. D. C. Giménez-López, J. P. Garrahan, X. Lin, M. Schröder, N. R. Champness, P. H. Beton, Random Tiling and Topological Defects in a Two-Dimensional Molecular Network, Science **322**, 1077–1081 (2008).

40. J. L Jacobsen, F. Alet, Semiflexible Fully Packed Loop Model and Interacting Rhombus Tilings, Physical Review Letters **102**, 145702 (2009).

41. L. Savary, L. Balents, Quantum spin liquids: a review. Reports on Progress in Physics **80**, 016502 (2016).

42. K. W. Plumb, J. Hirtesh, J. Changlani, A. Scheie, Shu Zhang, J. W. Kriza, J. A. Rodriuez-Rivera, Yiming Qui, B. Winn, R. J. Cava, C. L. Broholm, Continuum of quantum fluctuations in a three-dimensional S=1 Heisenberg magnet. https://arxiv.org/abs/1711.07509 (2017).

43. M. M. Koza, M. R. Johnson, R. Viennois, H. Mutka, L. Girard, D. Ravot, Breakdown of phonon glass paradigm in La- and Ce-filled Fe_4Sb_{12} skutterudites. Nature Materials **7**, 805–810 (2008).

44. T. Shimojima, Y. Shibata, K. Ishizaka, T. Kiss, A. Chainani, T. Yokoya, T. Togashi, X.-Y. Wang, C. T. Chen, S. Watanabe, J. Yamaura, S. Yonezawa, Y. Muraoka, Z. Hiroi, T. Saitoh, S. Shin, Interplay of Superconductivity and Rattling Phenomena in β-Pyrochlore KOs_2O_6 Studied by Photoemission Spectroscopy. Physical Review Letters **99**, 117003 (2007).

45. R. De Pape, G. Ferey, A new form of FeF_3 with the pyrochlore structure: Soft chemistry synthesis, crystal structure, thermal transitions and structural correlations with the other forms of FeF_3. Materials Research Bulletin **21**, 971–978 (1986).

46. S. W. Kim, S.-H. Kim, P. S. Halasyamani, M. A. Green, K. P. Bhatti, C. Leighton, H. Das, C. J. Fennie, $RbFe^{2+}Fe^{3+}F_6$: Synthesis, structure, and characterization of a new charge-ordered magnetically frustrated pyrochlore-related mixed-metal fluoride. Chemical Science **3**, 741–751 (2012).

47. P. R. Willmott, D. Meister, S. J. Leake, M. Lange, A. Bergamaschi, M. Böge, M. Calvi, C. Cancellieri, N. Casati, A. Cervellino, Q. Chen, C. David, U. Flechsig, F. Gozzo, B. Henrich, S. Jäggi-Spielmann, B. Jakob, I. Kalichava, P. Karvinen, J. Krempasky, A. Lüdeke, R. Lüscher, S. Maag, C. Quitmann, M. L. Reinle-Schmitt, T. Schmidt, B. Schmitt, A. Streun, I. Vartiainen, M. Vitins, X. Wang, R. Wullschleger. The Materials Science beamline upgrade at the Swiss Light Source. Journal of Synchrotron Radiation **20**, 667–682 (2013).

48. J. Rodriguez-Carvajal, Recent advances in magnetic structure determination. Physica B **192**, 55–69 (1993).

49. C. Wilkinson, J. A. Cowan, D. A. A. Myles, F. Cipriani, G. J. McIntyre, VIVALDI - A Thermal-Neutron Laue Diffractometer for Physics, Chemistry and Materials Science. Neutron News **13**, 37–41 (2002).

50. J. W. Campbell, Q. Hao, M. M. Harding, N. D. Nguti, C. Wilkinson, LAUEGEN version 6.0 and INTLDM. Journal of Applied Crystallography **31**, 496-502 (1998).

51. J. R. Helliwell, J. Habash, D. W. J. Cruickshank, M. M. Harding, T. J. Greenhough, J. W. Campbell, I. J. Clifton, M. Elder, P. A. Machin, M. Z. Papiz, S. Zurek, The recording and analysis of synchrotron X-radiation Laue diffraction photographs. Journal of Applied Crystallography **22**, 483–497 (1989).

52. G. M. Sheldrick. A short history of SHELX. Acta Crystallographica Section A: Foundations of Crystallography **64**, 112–122 (2008).

53. J. Schefer, M. Könnecke, A. Murasik, A. Czopnik, Th. Strässle, P. Keller, N. Schlumpf, Single-crystal diffraction instrument TriCS at SINQ. Physica B **276-278**, 168–169 (2000).

54. V. Petricek, M. Dusek, L. Palatinus, Crystallographic Computing System JANA2006: General features. Zeitschrift für Kristallographie 229, 345-352 (2014).

55. J. R. Stewart, P. P. Deen, K. H. Andersen, H. Schober, J.-F. Barthélémy, J. M. Hillier, A. P. Murani, T. Hayes, B. Lindenau. Disordered materials studied using neutron polarization analysis on the multi-detector spectrometer, D7. Journal of Applied Crystallography **42**, 69–84 (2008).

56. S.-H. Lee, C. Broholm, W. Ratcliff, G. Gasparovic, Q. Huang, T. H. Kim, S.-W. Cheong, Emergent excitations in a geometrically frustrated magnet. *Nature* **418**, 856–858 (2002).